HHS Public Access

Author manuscript

Nat Chem. Author manuscript; available in PMC 2022 July 01.

Published in final edited form as:

Nat Chem. 2022 January ; 14(1): 85–93. doi:10.1038/s41557-021-00826-8.

Bottlebrush Polymers with Discrete Sidechains Display Stereochemistry- and Conformation-Dependent Biological Properties

Hung V.-T. Nguyen[†,φ], **Yivan Jiang**[†,φ], **Somesh Mohapatra**[§], **Wencong Wang**[†], **Jonathan C. Barnes**[†], **Nathan J. Oldenhuis**[†], **Kathleen K. Chen**[†], **Simon Axelrod**[§,‡], **Zhihao Huang**[†], **Qixian Chen**[†], **Matthew R. Golder**[†], **Katherine Young**[†], **Dylan Suvlu**[†], **Yizhi Shen**[†], **Adam P. Willard**[†], **Michael J. A. Hore**[⊥], **Rafael Gómez-Bombarelli**[§,*], **Jeremiah A. Johnson**[†,*]

[†]Department of Chemistry, Massachusetts Institute of Technology, 77 Massachusetts Avenue, Cambridge, Massachusetts 02139, United States

[§]Department of Materials Science and Engineering, Massachusetts Institute of Technology, 77 Massachusetts Avenue, Cambridge, Massachusetts 02139, United States

[‡]Department of Chemistry and Chemical Biology, Harvard University, 12 Oxford Street, Cambridge, Massachusetts 02138, United States

[⊥]Department of Macromolecular Science and Engineering, Case Western Reserve University, 10900 Euclid Avenue, Cleveland, Ohio 44106, United States

Abstract

Chirality and molecular conformation are central components of life: biological systems rely on stereospecific interactions between discrete (macro)molecular conformers, and the impacts of stereochemistry and rigidity on the properties of small molecules and biomacromolecules have been intensively studied. Nevertheless, how these features affect the properties of synthetic macromolecules has received comparably little attention. Herein, we leverage iterative exponential growth (IEG) and ring-opening metathesis polymerization (ROMP) to produce water-soluble, chiral bottlebrush copolymers (CBPs) from two enantiomeric pairs of macromonomers (MMs) of differing rigidity. Remarkably, conformationally flexible, mirror-image CBPs show several-fold differences in cytotoxicity, cell uptake, blood pharmacokinetics, and liver clearance; comparably rigid mirror-image CBPs show no differences. These observations are rationalized with a simple model that correlates greater conformational freedom with enhanced chiral recognition. Altogether, this work provides routes to the synthesis of chiral nanostructured polymers and suggests key roles for stereochemistry and conformational rigidity in the design of future biomaterials.

[*] jaj2109@mit.edu; rafagb@mit.edu.

Author Contributions. J.A.J., H.V.T.N., J.C.B., and Y.J. conceived the idea. H.V.T.N., Y.J., J.C.B., W.W., K.C., Z.H., and K.Y., performed the chemical syntheses and characterizations. H.V.T.N., J.C.B., N.J.O., Q.C., and M.R.G. performed biological studies. S.M., S.A., and R.G.B. conducted simulations. M.J.A.H. conducted SANS studies. D.S., Y.S., A.P.W., and J.A.J. designed and conducted coarse-grained simulations. J.A.J., H.V.T.N., and Y.J. wrote the manuscript. All authors discussed the results and edited the manuscript.

[φ]These authors contributed equally to this work.

Competing Interests Statement. The authors declare no competing interests.

Graphical Abstract

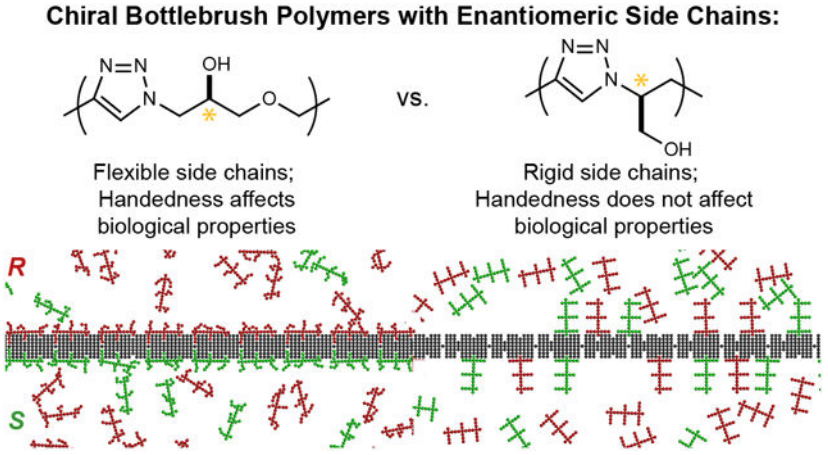

Introduction.

The complexity of life is derived from the chiral monomers that comprise biological polymers.[1] For example, the central dogma of molecular biology — which describes the flow of genetic information within a biological system — depends on molecular recognition processes that involve precise spatial orientation of chiral (macro)molecules.[2,3] Additionally, enzymes and receptors exert their functions via binding pockets with well-defined chiral shapes that are programmed from their primary sequence of chiral amino acids.[4] These structural features afford substrate specificity and assume crucial roles in diverse cellular processes including cellular trafficking, immune response, and molecular recognition. Moreover, specific absolute configurations are essential to nature's machinery: *e.g.,* most natural peptides have *L* configurations, while most sugars have *D* configurations.[5]

Given the ubiquitous presence of chirality in nature, it is not surprising that modern drug discovery, medicinal chemistry, and regulatory efforts have focused on stereochemically pure drug formulations.[6-8] While this standard for small molecules has existed for decades, less attention has been paid to the role of chirality in synthetic macromolecules (*e.g.,* polymers) designed for use in biological systems. Many commonly used synthetic polymers for biomaterials applications either lack stereogenic centers (*e.g.,* polyethylene glycol, PEG) or are employed as mixtures of stereoisomers.[9-12] Conjugation of PEG, *i.e.,* "PEGylation," is employed to stabilize biologics in clinical applications; in these cases, the biologic is a stereochemically defined macromolecule with a well-defined conformation (*e.g.,* a protein) while the PEG is an achiral, flexible appendage.[13-16]

Bioengineering strategies to produce chiral biomaterials have received significant attention; however, such approaches can currently only produce natural configurations and they suffer from a limited diversity of non-natural functionality.[17-19] Solid-phase synthesis and controlled polymerizations, by contrast, have enabled examination of the role of stereochemistry on the biological properties of materials primarily derived from amides (*e.g.,* peptides, peptoids, β-peptides, etc.) or other chiral pool sources, revealing

fascinating interplays between stereochemistry, conformation, and biological properties.[20-27] Self-assembled nanomaterials such as liposomes often contain chiral components (*e.g.*, cholesterol or derivatives thereof), though the effects of stereochemistry on the biological behaviors of such systems remains underexplored.[28-30] New strategies for the synthesis of water-soluble polymers with nanoscale dimensions and precisely controlled relative and absolute configurations and conformational rigidities are needed to explore the impacts of these features in biological settings.

Here, we introduce strategies for the synthesis of unimolecular norbornene-terminated macromonomers (MMs) with precise absolute configurations and spacings between hydroxyl sidechains, which influences conformational rigidity. Ring-opening metathesis polymerization (ROMP) of these MMs provides chiral bottlebrush polymers (CBPs) (Fig. 1a) that feature high water solubility and sizes similar to small proteins (hydrodynamic diameters, D_h, of ~ 3 nm). Molecular dynamics (MD) simulations, circular dichroism (CD) spectroscopy, and small-angle neutron scattering (SANS) were used to probe the conformations of the MMs and CBPs, revealing that the conformational preferences of the MMs (Fig. 1b) translate to the CBPs. Remarkably, CBPs with mirror image sidechains displayed configuration- and conformation-dependent behaviors in *in vitro* cytotoxicity, cell uptake, and red blood cell hemolysis assays, as well as in *in vivo* blood pharmacokinetics (PK) and biodistribution (BD) studies in mice. These observations are explained using a simple, intuitive model supported by simulations, showing that conformational flexibility can enhance chiral recognition when objects are not perfect “lock and key” binders. Our findings reveal an interplay between the stereochemistry and conformation of synthetic polymers that could potentially be leveraged to tailor the interactions of such materials with biological systems in the future, which should drive further development of synthetic strategies for precision polymers.

Results and Discussion.

Chiral bottlebrush polymer (CBP) design and synthesis.

We envisioned the synthesis of CBPs through replacement of the achiral PEG component of previously reported PEGylated bottlebrush polymers[31-36] with sidechains of defined absolute configurations (Fig. 1b). Toward this goal, we developed two iterative exponential growth (IEG)[37-40] protocols to produce discrete, mirror-image oligo-alcohols with either 2 atoms or 5 atoms between each main-chain triazole and orthogonally protected end groups. We hypothesized that the distance between planar triazoles in these “2 atom” versus “5 atom” macromolecules would impact their conformational rigidity (Fig. 1b, *vide infra*). The 2 atom IEG synthesis is described in Fig. 2a. Beginning from (*S*)-(+)-epichlorohydrin (>99.5% *ee*), **2A-S-O^{i}Pr-Dimer** was prepared in 11 total steps (9 linear) on the 9 g scale in 6% yield (see Supplementary Information for further details; Supplementary Fig. 1). Two IEG cycles of azidation, alkyne deprotection, and Cu-catalyzed azide-alkyne cycloaddition (CuAAC) yielded octamer **2A-*S*-O^{i}Pr-8mer** (Fig. 2b). Subsequent α- and ω-end-functionalizations with an *exo*-norbornene imide and tetraethylene glycol, respectively, yielded macromonomer (MM) **2A-*S*-O^{i}Pr-MM** (Fig. 2b). The same sequence of reactions beginning with (*R*)-(−)-epichlorohydrin provided enantiomer **2A-*R*-O^{i}Pr-MM,** while our

previously reported 5 atom IEG synthesis[38-40] coupled to analogous end functionalization reactions yielded 5 atom mirror-image MMs **5A-*R*-OAc-MM** and **5A-*S*-OAc-MM** (for full synthetic details and molecular characterizations, see Supplementary Figs. 1-22 and Supplementary Information Section C).

Each of these four MMs was subjected to ring-opening metathesis polymerization (ROMP), providing sidechain-protected CBPs (Fig. 3a; Supplemental Information Section C). Briefly, a given MM was exposed to Grubbs 3rd-generation bispyridyl (**G3**) complex in dichloromethane solvent using various MM:**G3** ratios to control the theoretical average backbone degrees of polymerization (DP). A significant difference in polymerization behavior between the 2 atom and 5 atom MMs was observed: while DP values up to 100 were readily achieved in the case of the 2-atom MMs (Supplementary Fig. 23), polymerizations of the 5 atom MMs stopped at much lower conversions for MM:**G3** > 25. This distinction suggests that the more flexible 5 atom MMs (*vide infra*) may adapt their conformation to coordinate to the Ru end of propagating chains, thus inhibiting polymerization, and agrees well with the biological investigations described later in this work. Given their high conversions, we moved forward with 4 different protected CBPs with DP = 25 (one for each MM listed above; see Supplementary Table 1 and Supplementary Figs. 24-32). The resulting CBPs displayed similar molecular weights and dispersities (Supplementary Table 1), confirming that any differences in properties within each enantiomeric pair must be due to stereochemistry. Global deprotection, dialysis against water, and subsequent lyophilization provided water-soluble (>40 mg CBP / mL H_2O) CBPs (Fig. 3b): **5A-*R*, 5A-*S*, 2A-*R*,** and **2A-*S*,** where again “5A” and “2A” refer to the number of atoms between triazoles in the CBP sidechains and *R* or *S* refer to their sidechain repeat unit absolute stereoconfiguration (Supplementary Figs. 33-56). **5A-*R*, 5A-*S*, 2A-*R*** and **2A-*S*** exhibited hydrodynamic diameters (D_h) of 3.2 ± 0.4 nm, 3.3 ± 0.7 nm, 2.8 ± 0.4 nm, and 2.5 ± 0.3 nm (Supplementary Table 1 and Supplementary Figs. 57-60), respectively, as determined by dynamic light scattering (1 mg CBP / 1 mL H_2O), confirming that, as expected, each CBP is the same size in solution as its isomer with mirror image sidechains while the 2 atom CBPs are slightly smaller due to the shorter length of their sidechains. These size ranges are similar to many natural and therapeutic biopolymers (*e.g.*, serum albumin diameter ~ 3.8 nm), suggesting that CBPs may be useful probes for exploring the role of synthetic polymer chirality and composition in biological systems. To facilitate such studies, 4 analogous CBPs labeled with the near-infrared fluorescent dye cyanine5.5 (Cy5.5) were prepared (see Supplemental Information Section C, Supplementary Figs. 61 and 62); the structures of these dye-labeled CBPs were indistinguishable from their non-fluorescent counterparts as determined by NMR spectroscopy (Supplementary Figs. 25-32 and 41-48) and gel permeation chromatography (Supplementary Fig. 24). Small-angle neutron scattering (SANS) data for the Cy5.5-labeled CBPs (see Supplemental Information section D, Supplementary Figs. 63 and 64) fitted with a flexible cylinder model revealed lengths of 9 nm and 10 nm and radii of 2.5 nm and 2.8 nm for the 2A and 5A CBPs, respectively.

Solution conformations of MMs and CBPs.

CD spectroscopy was used to study the conformations of deprotected MMs (Fig. 3c) and CBPs (Fig. 3d) in aqueous solutions (1 mg•mL^{-1}). While each enantiomeric pair of MMs displayed mirrored CD spectra as expected (Fig. 3c, Supplementary Fig. 65), the CD signals were much stronger for the 2 atom MMs (**2A-*S*-OH-MM** and **2A-*R*-OH-MM**), supporting our hypothesis that these structures would adopt more well-defined chiral secondary structures in aqueous solution compared to the 5 atom MMs. In addition, the CD spectra for the CBPs (Fig. 3d) closely resembled those of the MMs, suggesting that the solution conformations of the MMs are maintained following polymerization. SANS supported this notion: fitting the scattering data for **2A-*S*-OH-MM** with an excluded volume model revealed a radius of gyration, R_g = 1.2 nm. If no significant change in conformation occurs upon ROMP, then the expected radius of the CBP is $r_c \approx 2R_g$ = 2.4 nm. As noted above, the measured r_c of the 2A CBP **2A-*S*-Cy** was 2.5 nm, which is in excellent agreement (see Supplemental Information section D).

Molecular dynamics (MD) simulations were used to further probe the solution conformations of the deprotected MMs (Fig. 4 and Supplementary Figs. 66-S75; see Supplemental Information section E for details). Individual **2A-*R*-OH-MM** and **5A-*R*-OH-MM** chains were simulated with OpenMM using the OPLS forcefield and the TIP3P water model. Cubic simulation boxes of 9 nm were used, equivalent to a concentration of 0.08 M for each MM, with 25 ns equilibration and 1 μs production simulation times at 300 K. We averaged the results with sextuplicate simulations, one starting point obtained from low-energy configuration generated using random distance matrix approach in RDKit, and 5 from different uncorrelated starting points from a 100 ns simulation at 500K (Supplemental Information Section E1).

Analysis of root-mean-squared deviation (RMSD) and R_g^2 for all-atom trajectories indicates that **2A-*R*-OH-MM** has higher structural rigidity than **5A-*R*-OH-MM** (Fig. 4a). Moreover, despite having a longer contour length, **5A-*R*-OH-MM** has a relatively similar R_g, suggesting a more bundled geometry (Supplemental Information Section E2). The higher standard deviation of RMSD and R_g^2 for **5-A-*R*-OH-MM** are indicative of a broader distribution of conformational states. Analogous simulations for five different stereoisomers of each MM suggest that the 5-atom MMs are typically more flexible than their 2-atom counterparts (Supplemental Information Section E4 and Supplementary Figs 72-S74).

To connect the experimental CD spectra to the solution conformations of these MMs, we simulated the CD spectra by combining the structural information from MD with the optical properties of triazoles obtained from a quantum-chemical simulation (Supplemental Information Section E3). The excitation energy and transition dipole moment of triazole absorption are used to construct a model Hamiltonian at each frame. The coupling between monomers at each frame depends on their relative distance and orientation, and the magnitude of the CD signal depends on the structure of the relative orientations. The Hamiltonian is diagonalized to yield the polymer optical properties at each frame, which are then used to generate the CD spectrum and averaged along the trajectory. The simulated CD spectrum (Fig. 4b) generated with one excited state is qualitatively similar to the

experimentally obtained one (Fig. 3c) and suggestive of a more permanent secondary structure in **2A-*R*-OH-MM.**

Fig. 4c represents the radial distribution functions (RDFs) between the C5 atoms of consecutive triazoles (the carbon atoms bearing a hydrogen substituent) in **2A-*R*-OH-MM** and **5A-*R*-OH-MM.** Notably, the RDF for **2A-*R*-OH-MM** has defined peaks, which are indicative of well-defined solution conformations arising from hindered backbone rotation. By contrast, the peaks for **5A-*R*-OH-MM** are less defined and occur at greater distances, as expected from its longer and more flexible inter-triazole spacer, respectively.

A broader conformational analysis was performed by tracking the backbone dihedral angles of these MMs (24 for **2A-*R*-OH-MM** and 48 for **5A-*R*-OH-MM).** Time-structure Independent Component Analysis[41,42] (tICA) was used to decompose these high-dimensional structural features into two principal components that aggregate the time-distribution of dihedral angles by capturing the dominant slower, long-range motions. Markov state modeling (MSM) over these, followed by hierarchical clustering, was used to characterize the conformational landscape and partition it into discrete macrostates, *i.e.* conformers, connected by transition probabilities (Supplementary Figs. 73 and 74; SI Section E3). Fig. 4d-f show the tIC and MSM analysis, in which **2A-*R*-OH-MM** is observed to principally exist in a few distinct, long-lived conformations, while **5A-*R*-OH-MM** has a near-continuum of sub-states and a broader distribution. Bayesian analysis[43] further supports these observations and suggests that the conformational dynamics of **2A-*R*-OH-MM** can be described through a few discrete macrostates, while the behavior of **5A-*R*-OH-MM** requires many quickly interconverting conformers (Supplementary Fig. 75). Lastly, we used Continuous Chirality Measurement (CCM) to quantitate the deviation from mirror symmetry of these MMs along the MD trajectories.[44] It was found that the distributions of CCM values for **2A-*R*-OH-MM** and **5A-*R*-OH-MM** were nearly identical, which suggests that the MMs are similarly distinct from achiral analogues despite their very different conformational flexibilities and dynamics (Supplementary Fig. 76 and 77; Supplementary Section E4). Altogether, these results support the notion that **2A-*R*-OH-MM** is more conformationally rigid than **5A-*R*-OH-MM,** which translates to the CBPs as demonstrated through CD spectroscopy and SANS.

In vitro cell culture evaluation of CBPs.

Next, we set out to evaluate how the absolute configurations and conformational features of our CBP sidechains might impact their properties in biological assays. We note here that the only experimental variable for CBPs with mirror-image sidechains, e.g., **5A-*R*** and **5A-*S*,** is stereochemistry; any observed differences must therefore arise from different diastereomeric interactions in the chiral biological environment, as is well-known for enantiomeric small molecules and biomolecules. Thus, we began by incubating **5A-*R*** and **5A-*S*** with human umbilical vein endothelial cells (HUVEC), a well-established toxin-sensitive cell line. Strikingly, a 4.5-fold difference in the half-maximal inhibitory concentration (IC_{50}) was observed (Fig. 5a): IC_{50} = 0.9 ± 0.1 mg•mL^{-1} and 4.0 ± 0.2 mg•mL^{-1} for **5A-*R*** and **5A-*S*,** respectively, indicating that **5A-*R*** is significantly more cytotoxic ($p < 0.0001$) than its enantiomer. This greater cytotoxicity of **5A-*R*** was further observed using more robust

HeLa (cervical cancer; Fig. 5b) and MCF7 (breast cancer; Fig. 5c) adenocarcinoma cells at either 5 mg•mL^{-1} ($p < 0.0001$ for HeLa and $p = 0.0028$ for MCF-7) or 10 mg•mL^{-1} ($p = 0.0004$ for HeLa and $p = 0.0046$ for MCF-7). These results conclusively prove that the stereochemistry of these polymers impacts their cytotoxicity. Notably, the more rigid **2A-*R*** and **2A-*S*** CBPs had nearly identical cytotoxicities in these three cell lines (Fig. 5a-c), showing, as should be expected, that stereochemistry may not always lead to significant changes in a given property. Lastly, we note that all of these observed toxicities are low and comparable to analogous bottlebrush polymers with PEG sidechains.[45,46]

To further examine the role of the 5A CBP stereochemistry, we prepared polymer **"5A-*RS*"** via ROMP of a racemic mixture of the **5A-*R*-MM** and **5A-*S*-MM** (Supplementary Figs. 82 and 83). We note that this polymer sample consists of a large number of different molecules; even if the dispersity and stereochemistry of the polynorbornene backbone are neglected, there are 2^{25} or >33 million possible combinations of the *R* and *S* macromonomers for a DP = 25 CBP. Interestingly, **5A-*RS*** displayed similar toxicities toward HUVEC cells at all concentrations compared to **5A-*S*** (Supplementary Fig. 84). Given this finding, and the challenges of drawing conclusions from a large mixture of molecules, we focused the remainder of our studies on the stereochemically defined CBPs.

To determine if the cytotoxicity results correlated with cellular uptake, fluorescently labeled CBPs **5A-*R*-Cy, 5A-*S*-Cy, 2A-*R*-Cy,** and **2A-*S*-Cy** were incubated for 24 h with the same three cell lines at a non-toxic dose of 0.2 mg•mL^{-1}; total cell uptake was quantified by flow cytometry (Fig. 5d-f). Interestingly, **5A-*R*-Cy** was taken up 1.5-, 2.3-, and 2.4-fold more than **5A-*S*-Cy** in HUVEC, HeLa, and MCF7 cells, respectively ($p < 0.0001$ for all 3 cases), which correlates with its greater toxicity. Moreover, **2A-*R*-Cy** and **2A-*S*-Cy** displayed no statistical difference in uptake into HUVEC and MCF7 cells and only a ~5% difference in HeLa cells ($p = 0.0066$). To support that cell uptake rather than adhesion gave rise to the observed results, HUVEC cells were incubated for 24 h with **5A-*R*-Cy** or **5A-*S*-Cy** and subsequently subjected to confocal microscopy (Supplementary Fig. 85). The images revealed CBP distribution throughout the cytosol for both CBPs, confirming cellular uptake. Additionally, **5A-*R*** and **5A-*S*** were analyzed by a red blood cell hemolysis assay. At 10 mg•mL^{-1}, **5A-*R*** displayed a hemolysis level of 3.7 ± 0.6%, a 2.7-fold increase compared to **5A-*S*** (1.4 ± 0.2%, $p = 0.0184$, two-tailed *t* test, Supplementary Table 3), indicating a stereochemistry-based difference in membrane-rupture potential between these two polymers. Importantly, given the different conditions used for the cytotoxicity and hemolysis assays, a direct comparison between the concentrations observed to induce hemolysis and toxicity is not possible. We note again that these CBPs would be considered highly tolerated, as their hemolytic potency is comparable to other non-toxic materials.[47-49] Finally, to ensure the reproducibility of these findings, we repeated each of the cytotoxicity studies in triplicate, including re-synthesizing all of the MMs and CBPs from scratch, with different researchers conducting each synthesis, different batches of cells, and double-blinded researchers for the cellular assays.

In vivo pharmacokinetics (PK) and biodistribution (BD) in balb/c mice.

To determine if the unique properties of these CBPs translated from *in vitro* to *in vivo*, we conducted biodistribution (BD) and blood-compartment pharmacokinetics (PK) studies using healthy balb/c mice. Cy-labeled CBPs **5A-*R*-Cy, 5A-*S*-Cy, 2A-*R*-Cy,** and **2A-*S*-Cy** were each administered to healthy balb/c mice (n = 3 animals per group) via tail-vein injection (2 mg CBP in 200 μL of 5% aqueous glucose solution). BD data were acquired by *ex vivo* fluorescence imaging ($\lambda_{ex}/\lambda_{em}$ = 640/700 nm) of individual organs while blood PK data were obtained from fluorescence imaging of blood samples collected at different time points; percent injected doses (% IDs) were plotted versus time post-injection and fitted to a standard two-compartment model (Fig. 6a and 6b, Table 1).[50] Given their small size (< 5 nm; Supplementary Table 1), these CBPs cleared fairly rapidly from the blood compartment with < 1% ID observed 24 h post-injection. Nonetheless, remarkably, significant differences in blood PK were observed for **5A-*R*-Cy** compared to **5A-*S*-Cy**—the distribution (α) and clearance (β) half-lives ($t_{1/2}$) of **5A-*R*-Cy** were 5.7- and 4.2-fold shorter than for **5A-*S*-Cy** (Table 1). By contrast, the blood PK $t_{1/2}$ values for **2A-*R*-Cy** and **2A-*S*-Cy** were similar (Fig. 6b and Table 1). Interestingly, while the liver was the major clearance route for all of these CBPs, **5A-*R*-Cy** cleared much faster (Fig. 6c, Supplementary Fig. 87). For example, peak liver accumulation of **5A-*R*-Cy** was achieved ~6 h post-injection while **5A-*S*-Cy** did not reach peak liver accumulation until ~24 h (Fig. 6c, Supplementary Fig. 87). The 2 atom CBPs both displayed comparably delayed liver accumulation (maximum observed values at ~72 h) with no significant difference between the two (Supplementary Fig. 87).

Altogether, our results conclusively show that **5A-*R*** stands out compared to **5A-*S*** in nine different biological assays involving different conditions: it displays a shorter blood compartment $t_{1/2}$, faster liver clearance, enhanced red blood cell hemolysis, more rapid cell uptake in three cell lines, and greater cytotoxicity in three cell lines. Moreover, **2A-*R*** and **2A-*S*** do not display large or any differences in these same assays. To explain these observations and connect them to the differences in conformational flexibility between 5 atom and 2 atom CBPs as described above, we performed coarse-grained simulations of a model 2D chiral system comprising mirror image CBPs of varied sidechain flexibility and a chiral surface (“wall”) with binding sites for the CBPs (Supplementary Fig. 90). The latter is intended to mimic features of the complex chiral interfaces present in a biological system. We investigated the number of binding interactions of each CBP as a function of its flexibility, handedness (matched or mismatched), the strength of attractive forces between the CBP and the wall (ε), and the spacing of the binding sites on the wall (d_{wall}). These simulations revealed an intuitive yet, to our knowledge, unreported interplay between chirality and conformational flexibility that agrees well with our results. Specifically, when the surface binding sites are set at the optimal distance for CBP sidechain binding (d_{wall} = 1.00, Supplementary Fig. 90), then the more rigid CBPs occupy more surface binding sites, lacking the entropic penalties incurred for binding of the flexible CBPs; this finding is analogous to the well-known “lock-and-key” model of ligand binding. Strikingly, however, this trend is reversed when the chiral surface spacings are varied away from an ideal fit with the CBP sidechains (d_{wall} = 1.10, Supplementary Fig. 90). In this case, the rigid CBPs cannot adapt their conformation to fit the surface binding sites, leading to minimal interactions and, importantly, little differences between enantiomers. By contrast,

the flexible CBPs can explore more conformational space, adapting their sidechains to bind to the surface, which also gives rise to enantioselective differentiation: the flexible CBP of the matched handedness occupies more binding sites than its enantiomer. In other words, when the lock-and-key does not apply, as we expect to be the case for our CBPs as they are not designed to bind a specific target and they display similar properties across multiple biological assays under different conditions, conformational flexibility (e.g., of **5A-*R*** and **5A-*S*** compared to **2A-*R*** and **2A-*S***) can amplify chiral recognition.

Conclusion.

Herein, we report strategies for the synthesis of CBPs with tunable sidechain absolute configurations and rigidities, leveraging IEG methods to prepare “2 atom” and “5 atom” oligotriazole-based mirror-image MMs with variable backbone rigidity. ROMP of these MMs provides CBPs with stereochemistries and conformations that reflect their MMs. Striking differences were observed in terms of the polymerization behavior of these MMs, the conformations of both the MMs and CBPs, and the *in vitro* and *in vivo* biological properties of the CBPs. Most notably, 5 atom IEG CBPs with *R* sidechain stereoconfigurations displayed unique cytotoxicity, cell uptake, PK, and BD compared to its isomer with mirror image sidechains and its 2 atom IEG counterparts. To explain these observations, coarse-grained simulations were used to propose a model wherein the increased conformational flexibility of 5-atom CBPs amplifies the diastereomeric interactions with biomolecules. Altogether, this work establishes both chirality and conformational rigidity as parameters that should be considered for the development of next-generation synthetic polymers for biomaterials applications.

Methods.

General Procedure for Bottlebrush Polymer Syntheses.

Note: All ring-opening metathesis polymerization (ROMP) reactions for bottlebrush polymer syntheses were performed in a glovebox under N_2 atmosphere, following the same general procedure, which was modified from previous reports.[45,46]

5A-Poly-R and 5A-Poly-S: **5A-Poly-R.—**To a vial containing a stir bar, **5A-*R*-OAc-MM** (33.9 mg, 16.1 μmol, 25.0 eq) was added. To another vial, a solution of **G3** (0.02 M in DCM) was freshly prepared. DCM (289 μL) was then added to the MM vial, followed by the addition of **G3** solution (32.1 μL, 0.64 μmol, 1.0 eq) to give the desired MM:**G3** ratio of 25:1, while achieving a total MM concentration of 0.05 M, affording a yellow solution. The reaction mixture was allowed to stir for 12 hours at room temperature. To quench the polymerization, a drop of ethyl vinyl ether was then added, and an aliquot was taken out for GPC analysis. This procedure was also implemented for the synthesis of the **5A-Poly-*S***.

2A-Poly-R and 2A-Poly-S: **2A-Poly-R.—**To a vial containing a stir bar, **2A-*R*-O^{i}Pr-MM** (33.9 mg, 16.1 μmol, 25.0 eq) was added. To another vial, a solution of **G3** (0.02 M in DCM) was freshly prepared. DCM (289 μL) was then added to the MM vial, followed by the addition of **G3** solution (32.1 μL, 0.64 μmol, 1.0 eq) to give the desired MM:**G3** ratio of 25:1, while achieving a total MM concentration of 0.05 M, affording a yellow solution.

The reaction mixture was allowed to stir for 12 hours at room temperature. To quench the polymerization, a drop of ethyl vinyl ether was then added, and an aliquot was taken out for GPC analysis. This procedure was also implemented for the synthesis of the **2A-Poly-*S*.**

CBP synthesis.—Upon quenching of the ROMP reaction mixture, the reaction solution was transferred into a 40 mL vial using 10 mL of a 1:1 mixture of DCM and MeOH. Excess potassium carbonate (~1 g) was then added, and the mixture was stirred for 5 hours. The solvent was removed via rotary evaporation, and 10 mL of a 1:1 mixture of acetone and water were added. Excess potassium carbonate (~1 g) was then added, and the mixture was stirred overnight. The sample was then transferred into an 8 kD MWCO dialysis tubing (Spectrum Laboratories) and dialyzed against water (3 × 500 mL, solvent exchange every 6 hours). The collected solution was lyophilized, affording the product CBP as an off-white solid for **5A-*R*, 5A-*S*, 5A-*RS*, 2A-*R*, 2A-*S*** and a blue solid for **5A-*R*-Cy, 5A-*S*-Cy, 2A-*R*-Cy, 2A-*S*-Cy.**

Cell culture.—MCF7 cells (HTB-22, ATCC) and HeLa cells (CCL-2, ATCC) were cultured in DMEM media (ATCC) supplemented with 10% fetal bovine serum (FBS, VWR) and 1% penicillin/streptomycin (Thermo Fisher Scientific). Human umbilical vein endothelial cells (HUVEC, CC-2935, Lonza) were cultured in EGM^+ media (Lonza) supplemented with 1% penicillin/streptomycin using collagen-coated flasks (Corning). All cells were housed in 5% CO_2 humidified atmosphere at 37 °C. Cell lines were authenticated with STR profiling and tested negative for mycoplasma contamination prior to the study.

Animal usage.—All experiments involving animals were reviewed and approved by the MIT Committee for Animal Care (CAC). BALB/c mice (n = 3, female, 8–12 weeks old, Taconic) were used for pharmacokinetic and biodistribution studies after having receiving an alfalfa-free diet (TestDiet) for at least 2 weeks to minimize auto-fluorescence. Mice were housed in static microisolator caging. The room temperature is set at 70 °F with the room monitoring alarms set at ± 2 °F; relative humidity is maintained at 30–70%. A 14-hour light/10-hour dark cycle is used. Cages have hardwood chip bedding and a nestlet. Cage bottoms are changed at least once each week (twice if housing three or more adult mice). Cages are spot checked daily for excessively dirty cages. Food and water are provided *ad libitum.* Water bottles are replaced with clean ones at least once each week.

Supplementary Material

Refer to Web version on PubMed Central for supplementary material.

Acknowledgements.

We thank the Army Research Office (W911NF-17-1-0521) and the National Institutes of Health (R01-CA220468-01 and Postdoctoral Fellowships for M.R.G. and N.J.O.) for support of this work. We thank the National Science Foundation (Graduate Research Fellowship for H.V.-T.N.). This work was supported in part by the Koch Institute Support (core) Grant P30-CA14051 from the National Cancer Institute. We acknowledge the support of the National Institute of Standards and Technology, U.S. Department of Commerce, in providing the neutron research facilities used in this work. We also thank Dr. Julia Zhao for assistance with Figure 1. We thank Prof. S. E. Denmark and Dr. A. F. Zahrt for helpful discussions.

Data Availability.

All data supporting the findings of this study are available within the Article and its Supplementary Information and can also be obtained from the corresponding author upon reasonable request.

References.

1. Alberts B et al. Molecular biology of the cell 6th edition. Garland Science (2014).
2. Bustamante C, Cheng W & Mejia YX Revisiting the central dogma one molecule at a time. Cell 144, 480–497 (2011). [PubMed: 21335233]
3. Schneider-Poetsch T & Yoshida M Along the central dogma—controlling gene expression with small molecules. Annu. Rev. Biochem 87, 391–420 (2018). [PubMed: 29727582]
4. Breslow R Artificial enzymes. Science 218, 532–537 (1982). [PubMed: 7123255]
5. Breslow R & Cheng Z-L On the origin of terrestrial homochirality for nucleosides and amino acids. Proc. Natl. Acad. Sci. U. S. A 106, 9144–9146 (2009). [PubMed: 19478058]
6. FDA's policy statement on the development of new stereoisomeric drugs. Chirality 4, 338–340 (1992). [PubMed: 1354468]
7. Smith SW Chiral toxicology: it's the same thing…only different. Toxicol. Sci 110, 4–30 (2009). [PubMed: 19414517]
8. Brooks WH, Guida WC & Daniel KG The significance of chirality in drug design and development. Curr. Top. Med. Chem 11, 760–770 (2011). [PubMed: 21291399]
9. Shi J, Votruba AR, Farokhzad OC & Langer R Nanotechnology in drug delivery and tissue engineering: from discovery to applications. Nano Lett. 10, 3223–3230 (2010). [PubMed: 20726522]
10. Kakkar A, Traverso G, Farokhzad OC, Weissleider R & Langer R Evolution of macromolecular complexity in drug delivery systems. Nat. Rev. Chem 1, 0063 (2017).
11. Elsabahy M, Heo GS, Lim S-M, Sun G & Wooley KL Polymeric nanostructures for imaging and therapy. Chem. Rev 115, 10967–11011 (2015). [PubMed: 26463640]
12. Washington MA et al. The impact of monomer sequence and stereochemistry on the swelling and erosion of biodegradable poly(lactic-co-glycolic acid) matrices. Biomaterials 117, 66–76 (2017). [PubMed: 27936418]
13. Jokerst JV, Lobovkina T, Zare RN & Gambhir SS Nanoparticle PEGylation for imaging and therapy. Nanomedicine 6, 715–728 (2011). [PubMed: 21718180]
14. Otsukaa H, Nagasaki Y & Kataoka K PEGylated nanoparticles for biological and pharmaceutical applications. Adv. Drug Deliv. Rev 64, 246–255 (2012).
15. Knop K, Hoogenboom R, Fischer D & Schubert US Poly(ethylene glycol) in drug delivery: pros and cons as well as potential alternatives. Angew. Chem. Int. Ed. Engl 49, 6288–6308 (2010). [PubMed: 20648499]
16. Kolate A et al. PEG—a versatile conjugating ligand for drugs and drug delivery systems. J Control Release 192, 67–81 (2014). [PubMed: 24997275]
17. Kiick KL, Saxon E, Tirrell DA & Bertozzi CR Incorporation of azides into recombinant proteins for chemoselective modification by the Staudinger ligation. Proc. Natl. Acad. Sci. U. S. A 99, 19–24 (2002). [PubMed: 11752401]
18. Johnson JA, Lu YY, van Deventer JA & Tirrell DA Residue-specific incorporation of non-canonical amino acids into proteins: recent developments and applications. Curr. Opin. Chem. Biol 14, 774–780 (2010). [PubMed: 21071259]
19. van Hest JCM & Tirrell DA Protein-based materials, toward a new level of structural control. Chem. Commun 0, 1897–1904 (2001).
20. Lutz J-F, Ouchi M, Liu DR & Sawamoto M Sequence-controlled polymers. Science 341, 1238149 (2013). [PubMed: 23929982]

21. Simon RJ et al. Peptoids: a modular approach to drug discovery. Proc. Natl. Acad. Sci. U. S. A 89, 9367–9371 (1992). [PubMed: 1409642]
22. Wender PA et al. The design, synthesis, and evaluation of molecules that enable or enhance cellular uptake: peptoid molecular transporters. Proc. Natl. Acad. Sci. U. S. A 97, 13003–13008 (2000). [PubMed: 11087855]
23. Fowler SA & Blackwell HE Structure-function relationships in peptoids: recent advances toward deciphering the structural requirements for biological function. Org. Biomol. Chem 7, 1508–1524 (2009). [PubMed: 19343235]
24. Gestwicki JE, Cairo CW, Strong LE, Oetjen KA & Kiessling LL Influencing receptor–ligand binding mechanisms with multivalent ligand architecture. J. Am. Chem. Soc 124, 14922–14933 (2002). [PubMed: 12475334]
25. Yeom J et al. Chiral supraparticles for controllable nanomedicine. Adv. Mater 32, 1903878 (2020).
26. Wang X, Gan H & Sun T Chiral design for polymeric biointerface: the influence of surface chirality on protein adsorption. Adv. Func. Mater 21, 3276–3281 (2011).
27. Pooga M et al. Cell penetrating PNA constructs regulate galanin receptor levels and modify pain transmission *in vivo*. Nat. Biotechnol 16, 857–861 (1998). [PubMed: 9743120]
28. Pattni BS, Chupin VV & Torchilin VP New Developments in Liposomal Drug Delivery. Chem. Rev 115, 10938–10966 (2015). [PubMed: 26010257]
29. Metselaar JM et al. A Novel Family of l-Amino Acid-Based Biodegradable Polymer–Lipid Conjugates for the Development of Long-Circulating Liposomes with Effective Drug-Targeting Capacity. Bioconjugate Chem. 14, 1156–1164 (2003).
30. Gaspar MM, Perez-Soler R & Cruz ME Biological characterization of L-asparaginase liposomal formulations. Cancer Chemother. Pharmacol 38, 373–377 (1996). [PubMed: 8674161]
31. Sheiko SS, Sumerlin BS & Matyjaszewski K Cylindrical molecular brushes: synthesis, characterization, and properties. Prog. Polym. Sci 33, 759–785 (2008).
32. Verduzco R, Li X, Pesek SL & Stein GE Structure, function, self-assembly, and applications of bottlebrush copolymers. Chem. Soc. Rev 44, 2405–2420 (2015). [PubMed: 25688538]
33. Bielawski CW & Grubbs RH Living ring-opening metathesis polymerization. Prog. Polym. Sci 32, 1–29 (2007).
34. Johnson JA et al. Drug-loaded, bivalent-bottle-brush polymers by graft-through ROMP. Macromolecules 43, 10326–10335 (2010). [PubMed: 21532937]
35. Nguyen HV-T et al. Nitroxide-based macromolecular contrast agents with unprecedented transverse relaxivity and stability for magnetic resonance imaging of tumors. ACS Cent. Sci 3, 800–811 (2017). [PubMed: 28776023]
36. Barnes JC et al. Using an RNAi signature assay to guide the design of three-drug-conjugated nanoparticles with validated mechanisms, in vivo efficacy, and low toxicity. J. Am. Chem. Soc 138, 12494–12501 (2016). [PubMed: 27626288]
37. Binauld S, Damiron D, Connal LA, Hawker CJ & Drockenmuller E Precise synthesis of molecularly defined oligomers and polymers by orthogonal iterative divergent/convergent approaches. Macromol Rapid Commun. 32, 147–168 (2011). [PubMed: 21433136]
38. Barnes JC et al. Iterative exponential growth of stereo- and sequence-controlled polymers. Nat. Chem 7, 810–815 (2015). [PubMed: 26391080]
39. Jiang Y et al. Iterative exponential growth synthesis and assembly of uniform diblock copolymers. J. Am. Chem. Soc 138, 9369–9372 (2016). [PubMed: 27406892]
40. Golder MR et al. Stereochemical sequence dictates unimolecular diblock copolymer assembly. J. Am. Chem. Soc 140, 1596–1599 (2018). [PubMed: 29356516]
41. Pérez-Hernández G, Paul F, Giorgino T, De Fabritiis G & Noé F Identification of slow molecular order parameters for Markov model construction. J. Chem. Phys 139, 15102 (2013).
42. Schwantes CR & Pande VS Improvements in Markov State Model construction reveal many non-native interactions in the folding of NTL9. J. Chem. Theory Comput 9, 2000–2009 (2013). [PubMed: 23750122]
43. Bowman GR Improved coarse-graining of Markov state models via explicit consideration of statistical uncertainty. J. Chem. Phys 137, 134111 (2012). [PubMed: 23039589]

44. Dryzun C, Zait A & Avnir D Quantitative symmetry and chirality - a fast computational algorithm for large structures: proteins, macromolecules, nanotubes, and unit cells, J. Comput. Chem 32, 2526–2538 (2011). [PubMed: 21618558]
45. Sowers MA et al. Redox-responsive branched-bottlebrush polymers for in vivo mri and fluorescence imaging. Nat. Commun 5, 5460 (2014). [PubMed: 25403521]
46. Johnson JA et al. Core-clickable peg-branch-azide bivalent-bottle-brush polymers by romp: grafting-through and clicking-to. J. Am. Chem. Soc 133, 559–566 (2011). [PubMed: 21142161]
47. Choi J, Reipa V, Hitchins VM, Goering PL & Malinauskas RA Physicochemical Characterization and In Vitro Hemolysis Evaluation of Silver Nanoparticles. Toxicological Sciences 123, 133–143 (2011). [PubMed: 21652737]
48. Yu B, Yang Y, Liu Q, Zhan A, Yang Y & Liu H A Novel Star Like Eight-Arm Polyethylene Glycol-Deferoxamine Conjugate for Iron Overload Therapy. Pharmaceutics 12, 329 (2020).
49. Pachara S et al. Cytocompatibility Evaluation of a Novel Series of PEG-Functionalized Lactide-Caprolactone Copolymer Biomaterials for Cardiovascular Applications. Front. Bioeng. Biotechnol 8, 991 (2020). [PubMed: 32903548]
50. Rowland M, Benet LZ & Graham GG Clearance concepts in pharmacokinetics. J. Pharmacokinet. Biopharm 1, 123–136 (1973). [PubMed: 4764426]

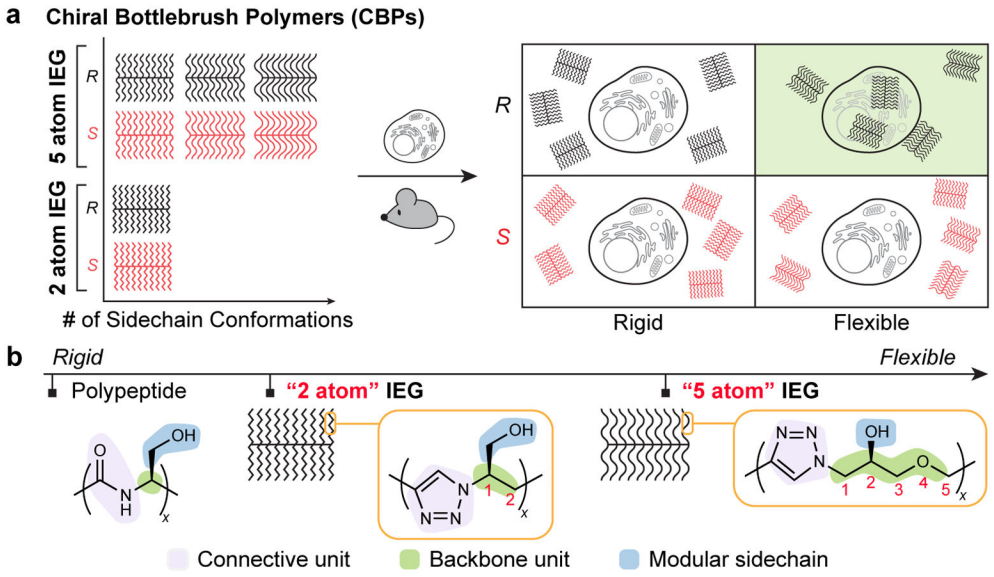

Figure 1. Conceptual design of this work.

a. Chiral bottlebrush polymers (CBPs) of varied conformational flexibility (*x*-axis) and absolute configuration (*y*-axis) derived from "5 atom" or "2 atom" iterative exponential growth (IEG) are synthesized. The 5 atom CBPs explore a greater conformational space compared to the 2 atom CBPs, as indicated in the upper left schematic. *In vitro* and *in vivo* biological studies reveal that the more flexible 5 atom CBP of a defined handedness (*R*) behaves differently (including enhanced cell uptake as indicated in the above right schematic) than its mirror image or more conformationally rigid 2 atom counterparts. **b.** Basic repeat units of the 5 atom and 2 atom IEG systems investigated in this work and a generic polypeptide repeat unit for comparison. CBPs of varied stereochemistry with oligotriazole sidechains featuring 2 atoms or 5 atoms between each triazole are shown to have significant differences in conformational flexibility and biological properties, providing a tunable platform to examine how the stereochemistry of synthetic, non-bioresemblant polymers impacts their function.

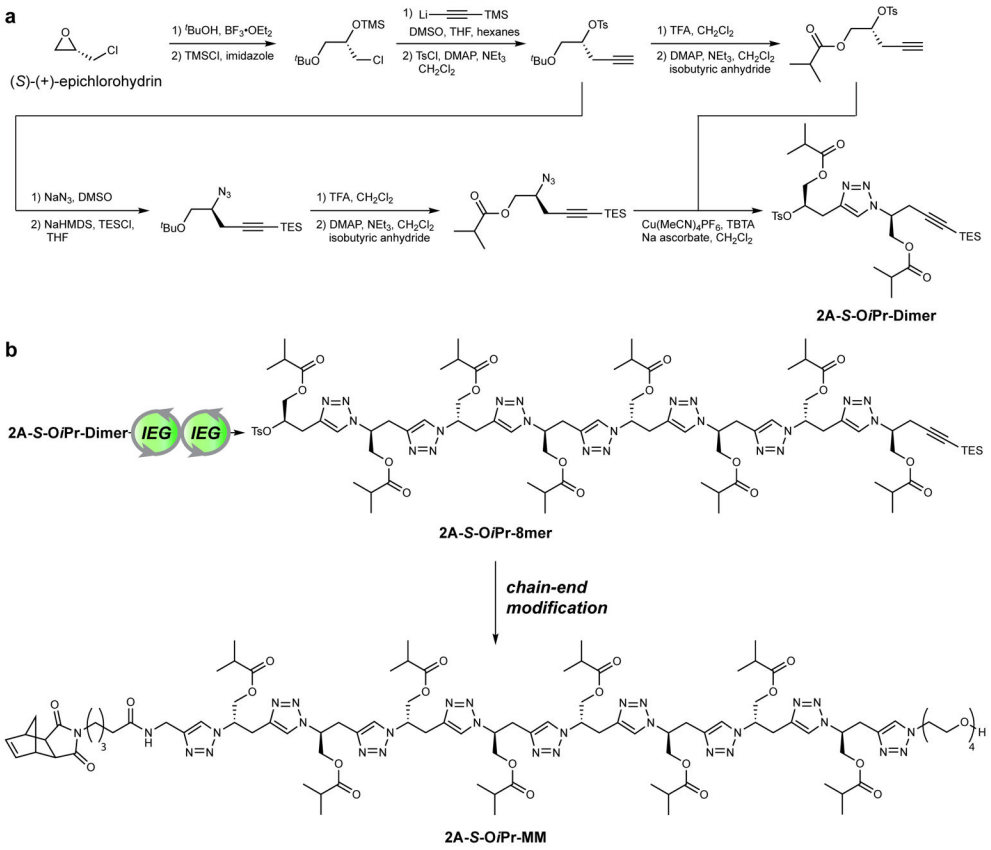

Figure 2. Scheme for "2 atom" iterative exponential growth (IEG) synthesis.

a. Commercially available (*S*)-(+)-epichlorohydrin is converted in 11 total steps, 9 longest-linear sequence, to IEG dimer **2A-*S*-O^{i}Pr-Dimer** (6% yield on the 9 g scale). See Supplemental Information Section C for full details. *Note:* The "*S*" label in **2A-*S*-O^{i}Pr-Dimer** refers to the source of the two stereogenic centers in this molecule rather than their actual labels based on Cahn-Ingold-Prelog priority rules, the latter of which would lead to one *R* and one *S* assignment. **b. 2A-*S*-O^{i}Pr-Dimer** is subjected to two iterative exponential growth (IEG) cycles, consisting of divergent azidation and alkyne deprotection then convergent copper-catalyzed azide-alkyne cycloaddition (CuAAC), to afford octamer **2A-*S*-O^{i}Pr-8mer. 2A-*S*-O^{i}Pr-8mer** is subsequently converted to macromonomer (MM) **2A-*S*-O^{i}Pr-MM** for ring-opening metathesis polymerization (ROMP) through coupling of an *exo*-norbornene derivative (left) and tetraethylene glycol (right) onto the chain ends. *Note*: due to the use of S_N2 reactions that invert the chain end stereochemistry, all of the stereogenic centers in **2A-*S*-O^{i}Pr-MM** are *S*.

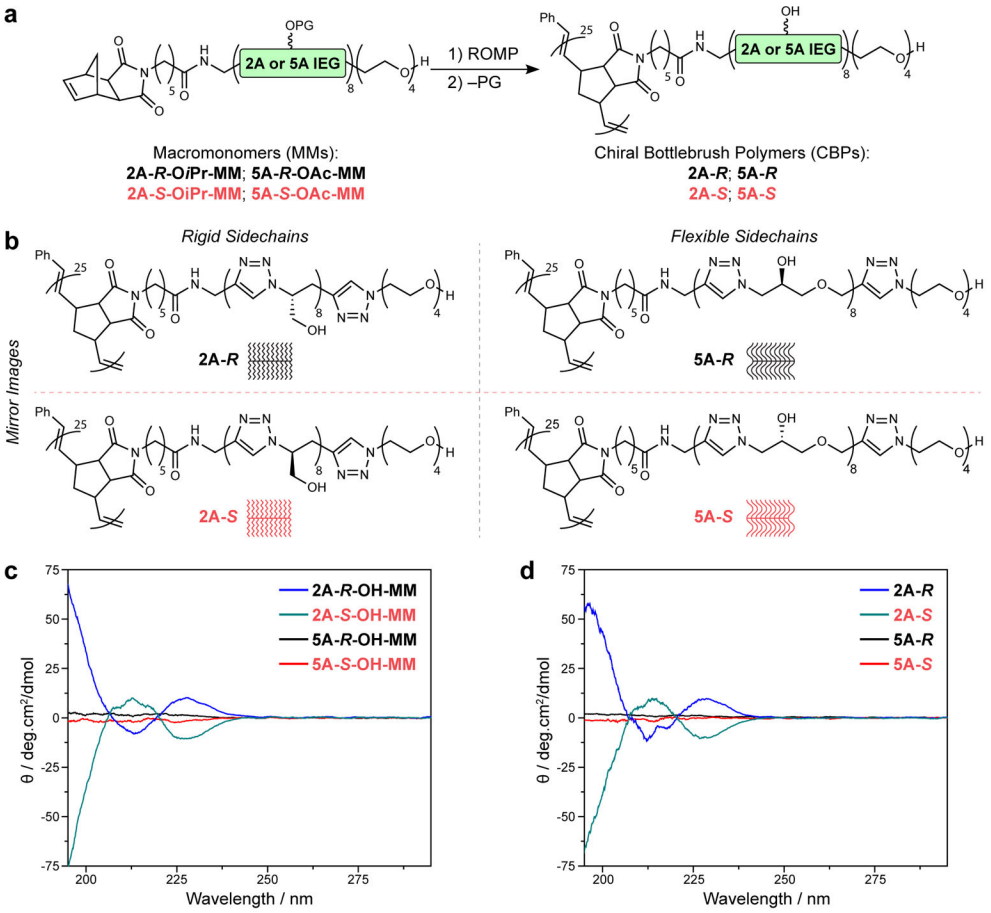

Figure 3. Chemical structures of 2 atom versus 5 atom MMs and CBPs and comparison of their CD spectra.

a. General structure of protected macromonomers (MMs) synthesized in this work. Ring-opening metathesis polymerization (ROMP) of these four MMs followed by sidechain deprotection affords CBPs with average backbone degrees of polymerization (DP) = 25. **b.** Chemical structures and schematics of the four CBPs studied in this work. These CBPs comprise two pairs of enantiomeric sidechains (*R* versus *S*) with varied sidechain rigidity (2 atom versus 5 atom). **c.** CD spectra for *deprotected* MMs in aqueous solution (1 mg•mL^{-1}). **d.** CD spectra for CBPs in aqueous solution (1 mg•mL^{-1}). The similarity between the CD spectrum for each CBP (**d**) and the MM from which it was constructed (**c**) suggests that conformational preferences of the MM are translated to the CBP upon ROMP, which was supported by SANS.

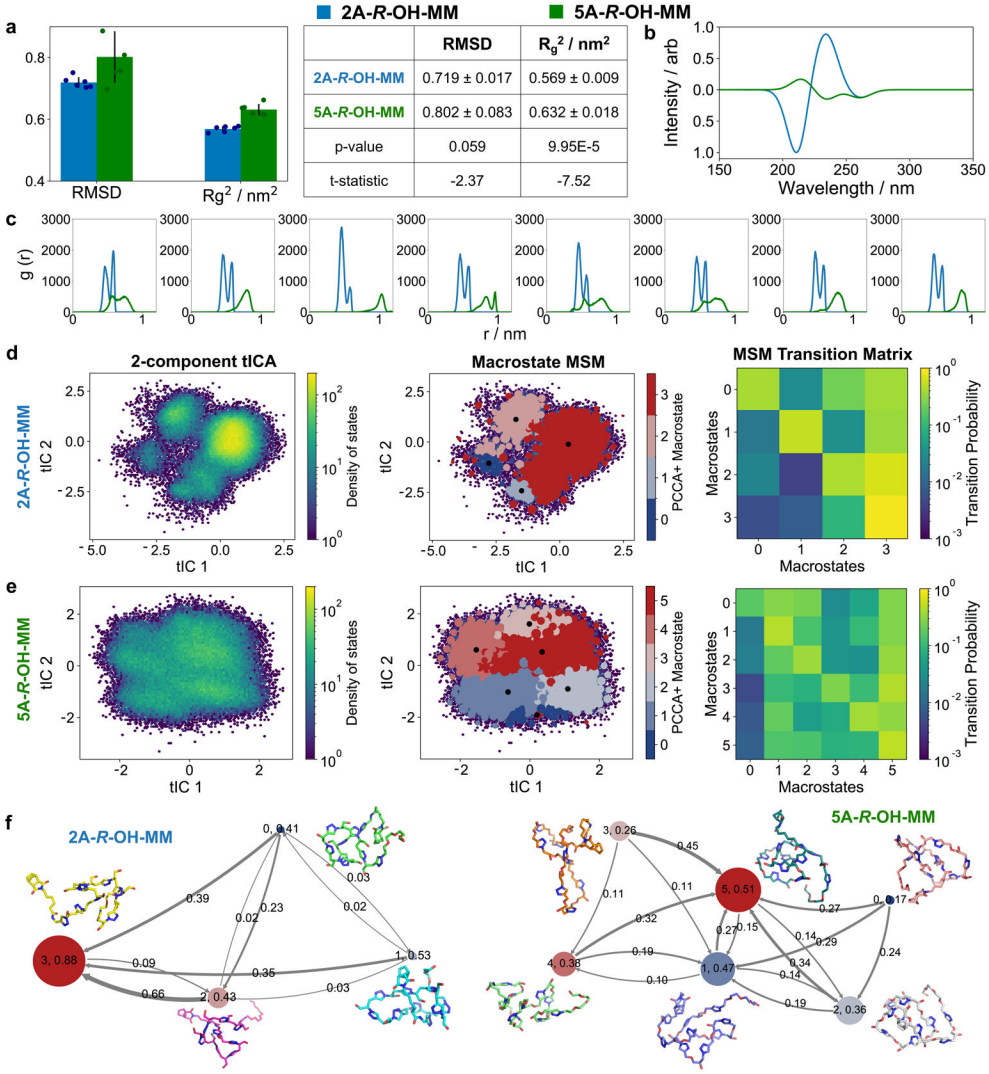

	RMSD	R_g^2 / nm^2
2A-*R*-OH-MM	0.719 ± 0.017	0.569 ± 0.009
5A-*R*-OH-MM	0.802 ± 0.083	0.632 ± 0.018
p-value	0.059	9.95E-5
t-statistic	-2.37	-7.52

Figure 4. Analysis of conformational flexibility of 2A-*R*-OH-MM and 5A-*R*-OH-MM using molecular dynamics simulations.

a. Comparison of mean (bar plot) and standard deviation (error bars) of root-mean-squared deviation (RMSD) and R_g^2 for **2A-*R*-OH-MM** and **5A-*R*-OH-MM** (n = 6 independent experiments). The mean, ± standard deviation of RMSD and R_g^2, are reported in the table, with Welch's two-sided t-test and p-values. **b.** *Ab initio* simulation to obtain circular dichroism spectra for **2A-*R*-OH-MM** and **5A-*R*-OH-MM**. **c.** Radial distribution functions for consecutive triazole units. Two-dimensional time-structure independent component analysis, Markov state model and macrostate transition matrix for **d. 2A-*R*-OH-MM** and **e. 5A-*R*-OH-MM**. **f.** Transition network between different MSM macrostates. Representative conformations for each macrostate have been sampled near the macrostate cluster center (black dots in macrostate MSM plots). The radii of macrostate nodes are proportional to the population of conformations in that macrostate. The arrows represent the direction of transition. All transition probabilities in the network are rounded to 2 decimal points, and not represented if less than 0.01 for **2A-*R*-OH-MM** and less than 0.10 for **5A-*R*-OH-MM**.

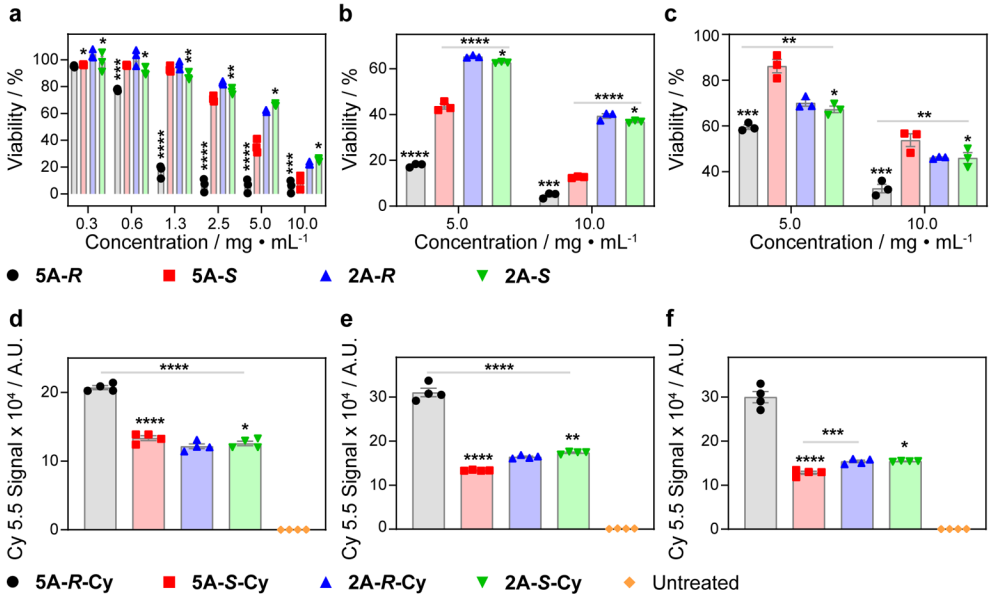

Figure 5. Cytotoxicity and uptake of CBPs in three different cell lines.

a. HUVEC cell viability (CellTiter-Glo assay) as a function of CBP concentration. **b.** HeLa cell viability (CellTiter-Glo assay) as a function of CBP concentration. **c.** MCF-7 cell viability (CellTiter-Glo assay) as a function of CBP concentration. **d.** Uptake of fluorescently labeled (Cy5.5) CBPs into HUVEC cells as quantified by flow cytometry. **e.** Uptake of fluorescently labeled (Cy5.5) CBPs into HeLa cells as quantified by flow cytometry. **f.** Uptake of fluorescently labeled (Cy5.5) CBPs into MCF-7 cells as quantified by flow cytometry. For cell viability assays, data are presented as mean ± SEM ($n = 3$ biologically independent samples). Flow cytometry data are presented as mean ± SEM ($n = 4$ biologically independent samples). Statistical comparisons were made using a two-tailed *t* test; comparisons were made between the *R* and *S* CBPs of the same IEG family, unless otherwise noted. *not significant, **$p < 0.05$, ***$p < 0.01$, ****$p < 0.0001$. The acquired *p* values are as the following. HUVEC viability: for **5A-*R*** and **5A-*S***, 0.5009 (10 mg•mL), 0.0021 (5 mg•mL), < 0.0001 (2.5 mg•mL), < 0.0001 (1.25 mg•mL), < 0.0001 (0.63 mg•mL), and 0.0005 (0.31 mg•mL); for **2A-*R*** and **2A-*S***, 0.1797 (10 mg•mL), 0.3157 (5 mg•mL), 0.0442 (2.5 mg•mL), 0.0426 (1.25 mg•mL), 0.0567 (0.63 mg•mL), and 0.2161 (0.31 mg•mL). HeLa viability: for **5A-*R*** and **5A-*S***, 0.0004 (10 mg•mL) and < 0.0001 (5 mg•mL); for **2A-*R*** and **2A-*S***, 0.2837 (10 mg•mL) and 0.4224 (5 mg•mL). For **5A-*S*** and **2A-*S***, < 0.0001 (10 mg•mL) and < 0.0001 (5 mg•mL). MCF-7 viability: for **5A-*R*** and **5A-*S***, 0.0046 (10 mg•mL) and 0.0028 (5 mg•mL); for **2A-*R*** and **2A-*S***, 0.7256 (10 mg•mL) and 0.4514 (5 mg•mL). For **5A-*R*** and **2A-*S***, 0.0115 (10 mg•mL) and 0.0118 (5 mg•mL). HUVEC cell uptake: for **5A-*R*** and **5A-*S***, < 0.0001; for **2A-*R*** and **2A-*S***, 0.4364. For **5A-*R*** and **2A-*S***, < 0.0001. HeLa cell uptake: for **5A-*R*** and **5A-*S***, < 0.0001; for **2A-*R*** and **2A-*S***, 0.0066. For **5A-*R*** and **2A-*S***, < 0.0001. MCF-7 cell uptake: for **5A-*R*** and **5A-*S***, < 0.0001; for **2A-*R*** and **2A-*S***, 0.9487. For **5A-*S*** and **2A-*R***, 0.0012. A.U. = arbitrary units.

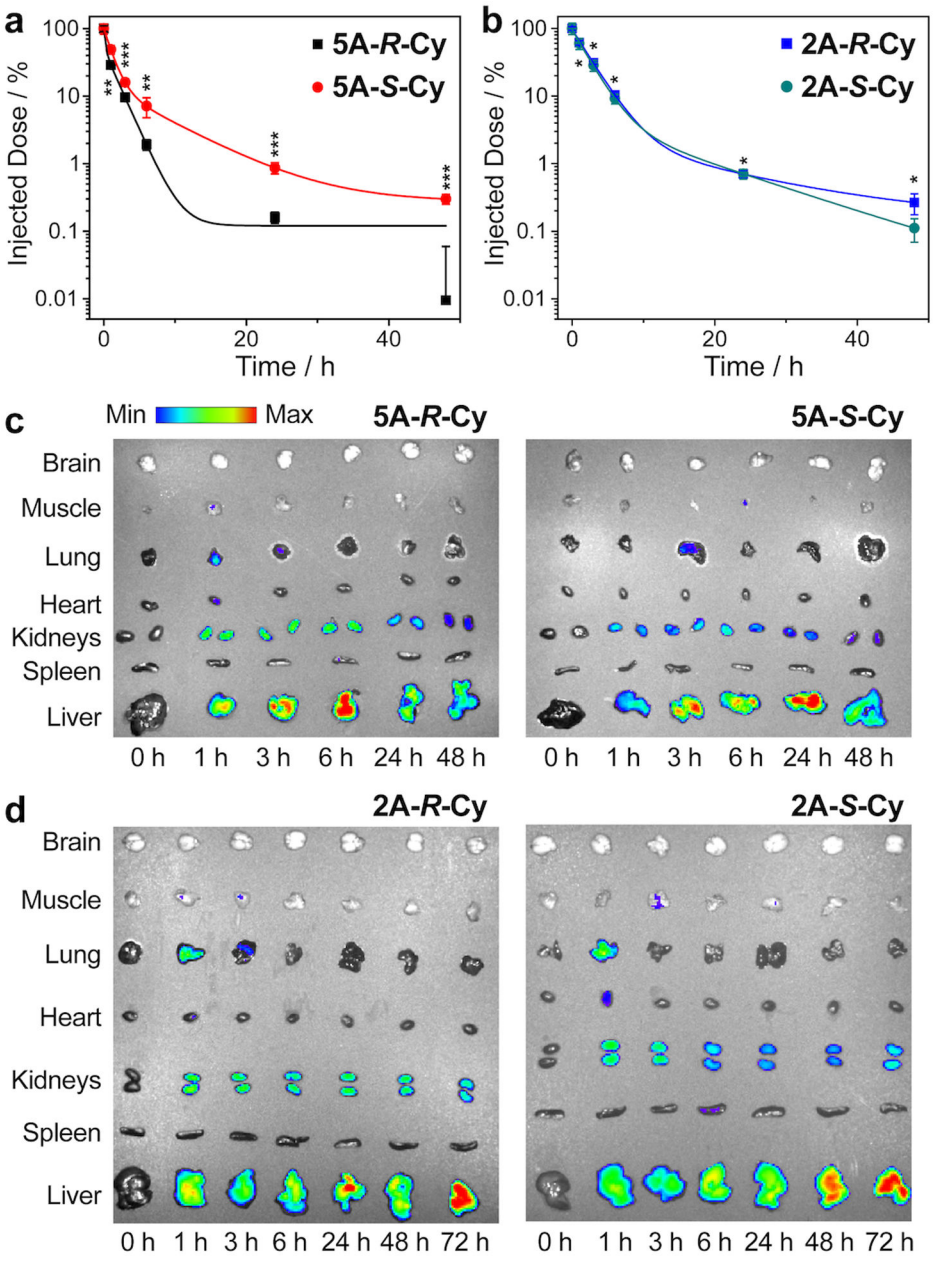

Figure 6. Blood compartment pharmacokinetics (PK) and *ex vivo* biodistribution (BD) for CBPs in healthy balb/c mice (n = 3 mice per treatment group).

a. PK for 5 atom CBPs, showing faster blood compartment clearance of **5A-*R*-Cy** compared to its enantiomer. **b.** PK for 2 atom CBPs, showing similar blood compartment clearance for these enantiomers. Data are presented as mean ± SEM ($n = 3$). Statistical comparisons were made using a two-tailed t test; comparisons were made between the R and S CBPs of the same IEG family at the same time point. *not significant, **$p < 0.05$, ***$p < 0.01$, ****$p < 0.0001$. The acquired p values are as the following: for **5A-*R*-Cy** and **5A-*S*-Cy**, 0.0105 (1 h), 0.0071 (3 h), 0.0186 (6 h), 0.0018 (24 h), and 0.0019 (48 h); for **2A-*R*-Cy** and **2A-*S*-Cy**, 0.8594 (1 h), 0.4217 (3 h), 0.2519 (6 h), 0.9470 (24 h), and 0.0549 (48 h). **c.** *Ex vivo* BD for 5 atom CBPs, showing faster liver accumulation (within ~6 h) and subsequent

clearance of **5A-*R*-Cy** compared to its enantiomer. **d.** *Ex vivo* BD for 2 atom CBPs, showing no differences between these enantiomers. Cy5.5 ($\lambda_{ex}/\lambda_{em}$ = 640/700 nm) was used for *ex vivo* fluorescence analysis. Scale bar = radiant efficiency $\frac{\mathrm{p}\,/\,sec\,/\,cm^2\,/\,sr}{\mu\mathrm{W}\,/\,\mathrm{cm}^2}$

Table 1.

Blood PK half-lives of CBPs in healthy balb/c mice.

	Distribution (α) Phase $t_{1/2}$ (h)	Clearance (β) Phase $t_{1/2}$ (h)	R^2 of Fit
5A-*R*-Cy	0.14	1.26	0.9196
5A-*S*-Cy	0.80	5.28	0.9999
2A-*R*-Cy	1.73	10.70	0.9948
2A-*S*-Cy	1.54	8.57	0.9957